1-1-2017

Evaluating Outer Segment Length as A Surrogate Measure of Peak Foveal Cone Density

Melissa A. Wilk
Medical College of Wisconsin

Brandon M. Wilk
Medical College of Wisconsin

Christopher S. Langlo
Medical College of Wisconsin

Robert F. Cooper
Marquette University

Joseph Carroll
Marquette University

Accepted version. *Vision Research,* Vol. 130 (January 2017): 57-66. DOI.

Evaluating Outer Segment Length as A Surrogate Measure of Peak Foveal Cone Density

Melissa A. Wilk
Department of Cell Biology, Neurobiology & Anatomy, Medical College of Wisconsin, Milwaukee, WI
Brandon M. Wilk
Department of Ophthalmology, Medical College of Wisconsin, Milwaukee, WI
Christopher S. Langlo
Department of Cell Biology, Neurobiology & Anatomy, Medical College of Wisconsin, Milwaukee, WI
Robert F. Cooper
Department of Biomedical Engineering, Marquette University, Milwaukee, WI
Joseph Carroll
Department of Cell Biology, Neurobiology & Anatomy, Medical College of Wisconsin, Milwaukee, WI

Vision Research, Vol 130 (January 2017): pg. 57-66. DOI.

Department of Ophthalmology, Medical College of Wisconsin, Milwaukee, WI
Department of Biomedical Engineering, Marquette University, Milwaukee, WI
Department of Biophysics, Medical College of Wisconsin, Milwaukee, WI

Abstract: Adaptive optics (AO) imaging tools enable direct visualization of the cone photoreceptor mosaic, which facilitates quantitative measurements such as cone density. However, in many individuals, low image quality or excessive eye movements precludes making such measures. As foveal cone specialization is associated with both increased density and outer segment (OS) elongation, we sought to examine whether OS length could be used as a surrogate measure of foveal cone density. The retinas of 43 subjects (23 normal and 20 albinism; aged 6–67 years) were examined. Peak foveal cone density was measured using confocal adaptive optics scanning light ophthalmoscopy (AOSLO), and OS length was measured using optical coherence tomography (OCT) and longitudinal reflectivity profile-based approach. Peak cone density ranged from 29,200 to 214,000 cones/mm^2 (111,700 ± 46,300 cones/mm^2); OS length ranged from 26.3 to 54.5 μm (40.5 ± 7.7 μm). Density was significantly correlated with OS length in albinism ($p < 0.0001$), but not normals ($p = 0.99$). A cubic model of density as a function of OS length was created based on histology and optimized to fit the albinism data. The model includes triangular cone packing, a cylindrical OS with a fixed volume of 136.6 μm^3, and a ratio of OS to inner segment width that increased linearly with increasing OS length ($R^2 = 0.72$). Normal subjects showed no apparent relationship between cone density and OS length. In the absence of adequate AOSLO imagery, OS length may be used to estimate cone density in patients with albinism. Whether this relationship exists in other patient populations with foveal hypoplasia (e.g., premature birth, aniridia, isolated foveal hypoplasia) remains to be seen.

Keywords: Fovea, Cone photoreceptor, Adaptive optics, Outer segment, Cone density

1. Introduction

The human fovea underlies the majority of our visual function, including color vision and high spatial acuity. While the fovea occupies only about 0.02% of the total retinal area, some 40% of primary visual cortex is devoted to processing signals from it (Hendrickson, 2005).

Several anatomical features distinguish the foveal region, namely an avascular zone (FAZ), the displacement of inner retinal neurons (forming the foveal pit), and a pronounced increase in cone density (with an absence of rod photoreceptors in the central fovea). Despite its importance for human vision, much remains to be discovered about how this structure develops, how it is disrupted during aging and disease, and how it interacts with central visual system structures to determine key features of visual function.

Several conditions are known to affect the development of the fovea. Individuals born prematurely have been shown to have smaller FAZs and foveal pits (Hammer et al., 2008, Wilk et al., 2014a and Yanni et al., 2012). In addition, patients with albinism or aniridia also have foveal hypoplasia (lack of a foveal pit) as well as reduced foveal cone specialization (Wilk et al., 2014a and Wilk et al., 2014b). Other cases of isolated foveal hypoplasia in the absence of albinism/aniridia have also been described (Perez et al., 2014 and Saffra et al., 2012). While cone specialization hasn't been studied in some of these populations, data from albinism suggests that the lack of a foveal pit would result in reduced cone packing at the fovea (Wilk et al., 2014b). Insights into the level of cone specialization in these subjects would not only give insight into foveal development, but also provide clues as to the cause of vision deficits in these individuals.

One of the key technological advances in our ability to study the human fovea has been non-invasive retinal imaging. For example, optical coherence tomography (OCT) can be used to examine foveal pit morphology (Chui et al., 2012, Dubis et al., 2012, Dubis et al., 2009, Hammer et al., 2008, Wagner-Schuman et al., 2011, Wilk et al., 2014b and Wilk et al., 2016) and the avascular zone (Braaf et al., 2013, Samara et al., 2015 and Wilk et al., 2016). In addition, adaptive optics (AO) imaging enables direct visualization of individual rod and cone photoreceptors (Dubra et al., 2011, Li et al., 2010, Putnam et al., 2005, Wilk et al., 2014b and Zhang et al., 2015). While there has been success in measuring peak cone density in normal populations (Putnam et al., 2005, Wilk et al., 2016, Wilk et al., 2014b and Zhang et al., 2015), the presence of nystagmus in a range of retinal diseases often precludes high-resolution imaging (Langlo et al., 2016 and Wilk et al., 2014b). With the goal of relating foveal cone structure to visual

Vision Research, Vol 130 (January 2017): pg. 57-66. DOI.

system function (Rossi and Roorda, 2010 and Williams and Coletta, 1987), these limitations represent an important barrier in vision research.

A review of foveal cone anatomy provides clues as to possible alternative strategies for estimating foveal cone density. As mentioned above, it is widely appreciated that the fovea contains the highest density of cone photoreceptors in the normal human retina, with estimates ranging from 80,000 to 300,000 (Curcio et al., 1990, Gao and Hollyfield, 1992, Putnam et al., 2005, Wilk et al., 2014b, Wilk et al., 2016, Yuodelis and Hendrickson, 1986 and Zhang et al., 2015). Moreover, it has been demonstrated by numerous investigators using ex vivo (Yuodelis & Hendrickson, 1986) and in vivo (Hammer et al., 2008, Liu et al., 2015, McAllister et al., 2010 and Wilk et al., 2014b) techniques that foveal cone outer segments (OS) are elongated relative to peripheral cones. It has been suggested that the elongation and increased packing of cones are directly linked (Diaz-Araya and Provis, 1992, Hendrickson and Yuodelis, 1984 and Provis et al., 2013). As the cones become tightly packed, the OS diameter decreases; since the OS appears to have constant volume (Hoang, Linsenmeier, Chung, & Curcio, 2002), the OS elongates to fit into the tight packing array. It is this concept that formed the basis for the present study. Here, we used AO scanning light ophthalmoscopy (AOSLO) and OCT to examine cone density and OS elongation in subjects with a range of cone densities. These data were then used to adapt a model for the relationship between peak density and OS length, which can be used to estimate foveal cone density from OS length in patients with albinism. Given the relative ease of measuring OS length compared to cone density, as well as the broader access to OCT compared to AO imaging devices, this could be a useful approach for vision scientists to characterize foveal cone specialization in difficult populations.

2. Methods

2.1. Subjects

This study followed the tenets of the Declaration of Helsinki and was approved by the Medical College of Wisconsin Institutional Review Board. Informed consent was obtained from all subjects (or adult

guardian of minors) after explanation of the nature and possible consequences of the study. Twenty-three subjects with normal vision (7 female, 16 male; 8–67 years of age) and 20 subjects with albinism (9 male, 11 female; 6–40 years of age) were recruited for this study (Table 1). A subset of the subjects had previously participated in studies by Wilk et al. (2014b) and/or Cooper, Wilk, Tarima, and Carroll (2016). All normal subjects except JC_0878 have also been described by Wilk et al. (2016). Each subject had one eye dilated and accommodation suspended using one drop each of Phenylephrine Hydrochloride (2.5%) and Tropicamide (1%) prior to imaging. Axial length, used for estimating the absolute scale of the retinal images, was measured using an IOL Master (Carl Zeiss Meditec, Dublin, CA).

Table 1. Subject demographics and cone specialization results.

Group	Subject	Age	Sex	Eye[a]	Axial length (mm)	Peak cone density (cones/mm^2)	OS length (μm)		
							Maximum[d]	Minimum[f]	2 mm
Normal	JC_0002	28	M	OD	24.72	147,600	44.2	33.1	14.7
	JC_0007[b]	37	M	OD	27.45	106,700	45.6	34.6	20.3
	JC_0138	25	F	OD	22.75	195,000	40.2	30.1	13.5
	JC_0200[b,c]	26	M	OD	24.72	128,600	45.1[e]	34.8	22.0
	JC_0571	25	M	OD	24.08	137,300	46.1	31.6	18.8
	JC_0616	23	M	OD	24.35	167,300	54.5[e]	34.6	21.0
	JC_0628	67	F	OD	22.92	165,100	47.8	34.6	21.8
	JC_0629	63	M	OD	23.29	160,700	47.6	36.1	19.5
	JC_0645	20	M	OD	23.76	177,500	45.2	34.6	22.2
	JC_0654	25	F	OD	23.57	214,000	47.6	36.1	20.3
	JC_0661	23	M	OD	25.52	132,200	44.5	34.6	21.4
	JC_0677[b,c]	24	F	OD	24.03	165,100	49.3	36.1	17.7
	JC_0692	40	M	OD	24.54	142,400	51.1[e]	39.1	21.4
	JC_0769[b]	21	F	OD	24.29	127,800	51.1[e]	37.6	22.9
	JC_0878[c]	8	F	OD	23.36	170,900	42.4[e]	34.6	18.0
	JC_0905[b,c]	21	M	OD	22.46	125,600	46.4	34.6	24.8
	JC_10119[c]	22	M	OD	25.9	108,100	47.6	37.6	24.8
	JC_10121[c]	23	M	OS	23.93	144,600	48.3	33.1	24.8
	JC_10145[c]	49	F	OD	24.66	120,500	45.9	36.1	22.9
	JC_10147[c]	13	M	OS	24.66	134,400	48.4	34.6	20.7
	JC_10311[c]	62	M	OD	22.86	153,400	46.8	33.1	22.9
	JC_10312[c]	15	M	OS	26.88	128,600	44.0	33.1	21.8
	JC_10329[c]	22	M	OS	24.46	127,800	46.6	36.1	24.8
Albinism	JC_0103[b]	20	M	OD	22.58	29,200	26.3	24.1	18.0[g]
	JC_0438[b]	23	M	OD	21.05	75,200	31.9	27.1	26.3[g]

Group	Subject	Age	Sex	Eye[a]	Axial length (mm)	Peak cone density (cones/mm^2)	OS length (μm)		
							Maximum[d]	Minimum[f]	2 mm
	JC_0456[b]	17	M	OD	23.62	100,100	41.5[e]	34.6	13.9
	JC_0492[b]	28	F	OD	23.62	81,800	35.5	33.1	26.3[g]
	JC_0493[b]	21	F	OD	22.33	89,100	37.6	33.1	21.8
	JC_0829[b]	10	F	OD	21.43	84,700	34.6	28.6	15.4
	DC_0831[b]	7	M	OD	21.38	82,500	33.0[e]	27.1	18.0
	KS_0935[b]	7	M	OD	20.77	126,400	39.4	33.1	20.3
	JC_10042	6	F	OD	21.96	46,000	31.8	25.6	21.8
	JC_10061	28	M	OD	24.8	45,300	30.6	25.6	15.8[g]
	JC_10074[b]	20	F	OD	23.53	44,600	33.4[e]	28.6	20.3
	JC_10081	11	F	OS	21.53	51,100	30.2	27.1	22.6[g]
	JC_10092	22	F	OD	22.78	62,100	28.0	24.1	16.5[g]
	JC_10093	17	M	OD	21.28	50,400	31.6	30.1	24.8[g]
	TC_10110	40	F	OS	22.99	111,000	39.0	33.1	20.3[g]
	JC_10192	6	F	OS	22.18	89,100	35.5	30.1	21.0[g]
	JC_10227	18	F	OD	22.82	78,900	34.2	30.1	19.2
	JC_10230	18	F	OS	20.15	46,000	30.6	27.1	18.8[g]
	JC_10278	14	M	OD	22.82	81,600	32.0	30.1	17.3[g]
	JC_10287	10	M	OD	21.69	47,500	27.7	25.6	20.3[g]

[a]OD = Right Eye; OS = Left Eye.
[b]Subject previously described by Wilk et al. (2014b).
[c]Subject previously described by Cooper et al. (2016).
[d]Maximum OS length from over 500-μm region.
[e]Foveal OS length measured from single B scan of volumetric OCT.
[f]Minimum OS length from over 500-μm region.
[g]OS length 2 mm either temporal or nasal from maximum OS length (not average of temporal and nasal).

2.2. Measuring foveal cone density

The foveal cone mosaic was imaged using confocal reflectance AOSLO (Dubra et al., 2011). The AOSLO image sequences were registered and averaged as previously described to create images with high signal-to-noise ratios (Cooper et al., 2011 and Dubra and Harvey, 2010). Peak cone density was estimated using a previously described method (Wilk et al., 2014b). Briefly, a region encompassing the peak density was cropped from the foveal images. Cones in the image were semi-automatically identified as previously described (Garrioch et al., 2012). The density at each pixel in the image was computed by counting the cones within variable window sizes. The densities at each pixel for all window sizes were averaged, and the pixel with the

greatest average density was considered the location of peak density. The density at this location was then measured using a 37 × 37 μm sampling window and recorded as the peak foveal cone density.

2.3. Estimating foveal outer segment (OS) length

High-resolution SD-OCT (Bioptigen, Research Triangle Park, NC) was performed on all subjects. Horizontal line scan sets were acquired (1000 A-scans/B-scan; 100–200 repeated B-scans; nominal scan length of 6 or 7 mm) through the foveal center. When a normal pit was absent (e.g., albinism), imaging was centered at the location of the incipient fovea (based on inspection of additional volumetric scans obtained). Line scans were registered and averaged as previously described to reduce speckle noise in the image (Tanna et al., 2010). The lateral image dimension was corrected for axial length by dividing the nominal scan width by the assumed axial length of the device (24 mm) times the subject's actual axial length. Processed line scans were cross-referenced with volumetric scans (ranging from 400 to 750 A-scans/B-scan and 100–250 B-scans over 6 × 6 or 7 × 7 mm nominally) to confirm that the location of apparent maximum OS length was encompassed in the line scan. In the eight subjects for whom this was not the case (Table 1), a single B-scan from the volume scan was used for analysis. In subjects with albinism lacking true OS elongation (n = 4), the fovea was identified by other features such as outer nuclear layer thickening or doming of the retina as described by McAllister et al. (2010).

Custom Java (Oracle Corporation, Redwood Shores, CA) software was written for analysis of OCT reflectance through use of longitudinal reflectivity profiles, or LRPs (OCT Reflectivity Analytics [ORA], Fig. A.1). Prior to analysis, each subject's image was resampled so that all images were the same scale and dimensions in both directions, and all LRPs were created over a 5-pixel (26.3 μm) width from the linear image. The location estimated to be the greatest OS length was manually selected for each image by a single observer (MAW). Consecutive LRPs were generated every 25 μm over a 500-μm region centered on this selection. For each LRP, the user selected the peaks corresponding to the EZ and IZ bands (Fig. 1). The distance between the two peaks for each LRP was calculated. A Gaussian was fit

Vision Research, Vol 130 (January 2017): pg. 57-66. DOI.

to the difference between peaks over the 500-μm width to generate an interpolated contour of OS length for this region. The reported maximum OS length is the maximum of the Gaussian fit for each subject. For more details on ORA, see Appendix A.

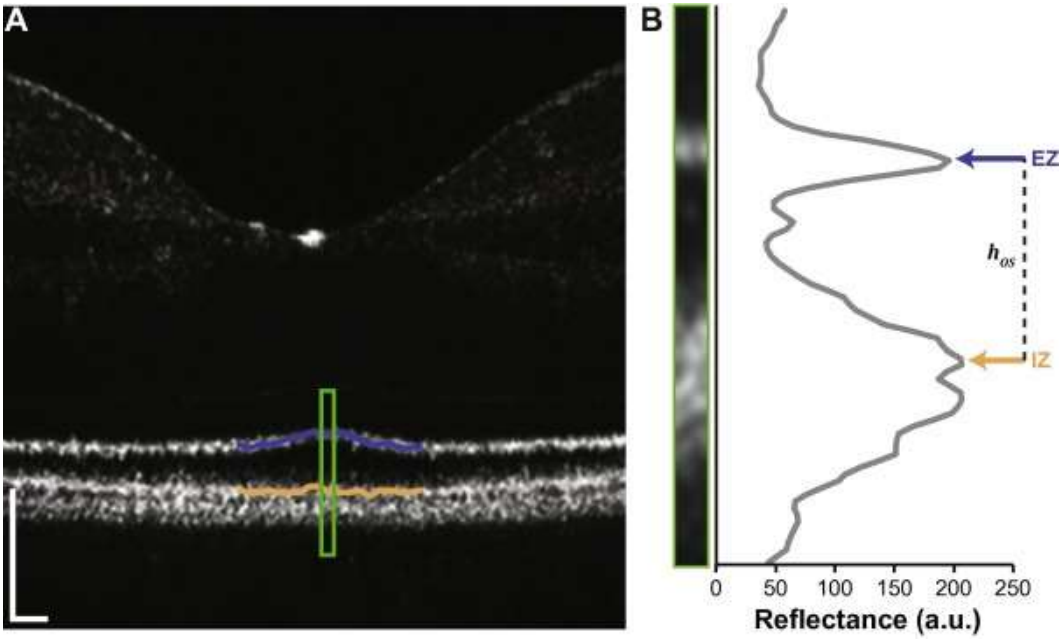

Fig. 1. OS length measured using LRP. (A) OCT in the linear display. Consecutive LRPs were created every 25 μm over a 500 μm region. By selecting the peaks for the EZ (blue) and IZ (orange), ORA creates the corresponding segmentation lines. The green box denotes the location of maximum OS length as determined from the Gaussian fit to the difference between the blue and orange segmentation points. (B) Foveal region outlined in green in (A) showing the location of peak OS length. An LRP (right) was generated over the width of the selection, allowing identification of the EZ (blue arrow) and IZ (orange arrow), with the OS length (h_{OS}) being the distance between them (dashed line). Scale bars = 100 μm.

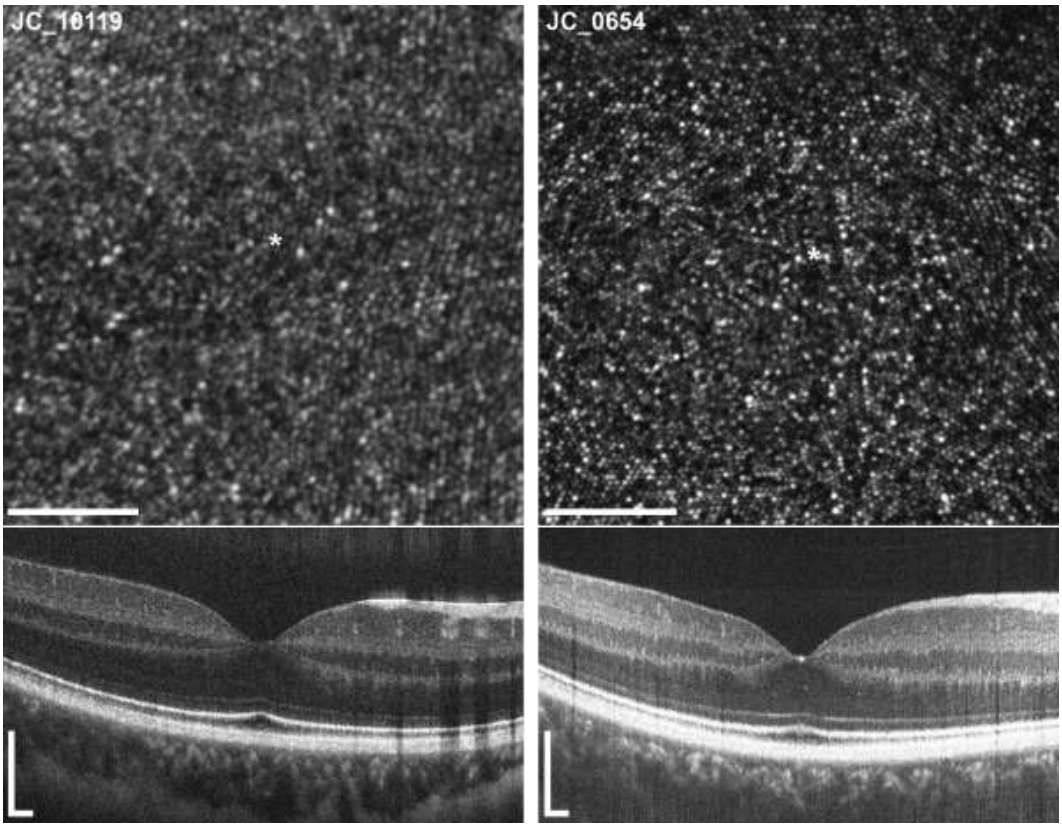

Fig. 2. Range in normal foveal cone specialization. Left panel shows the foveal cone mosaic and OCT from a normal subject with low peak cone density (JC_10119, peak density = 108,100 cones/mm^2). The images on the right are from the normal subject with highest peak cone density (JC_0654, peak density = 214,000 cones/mm^2). Despite differences in peak cone density, the OS length for both of these subjects is 47.6 μm. The asterisk (∗) in the top panel marks the estimated location of peak cone density for each subject. AO image scale bars = 50 μm; OCT scale bars = 200 μm.

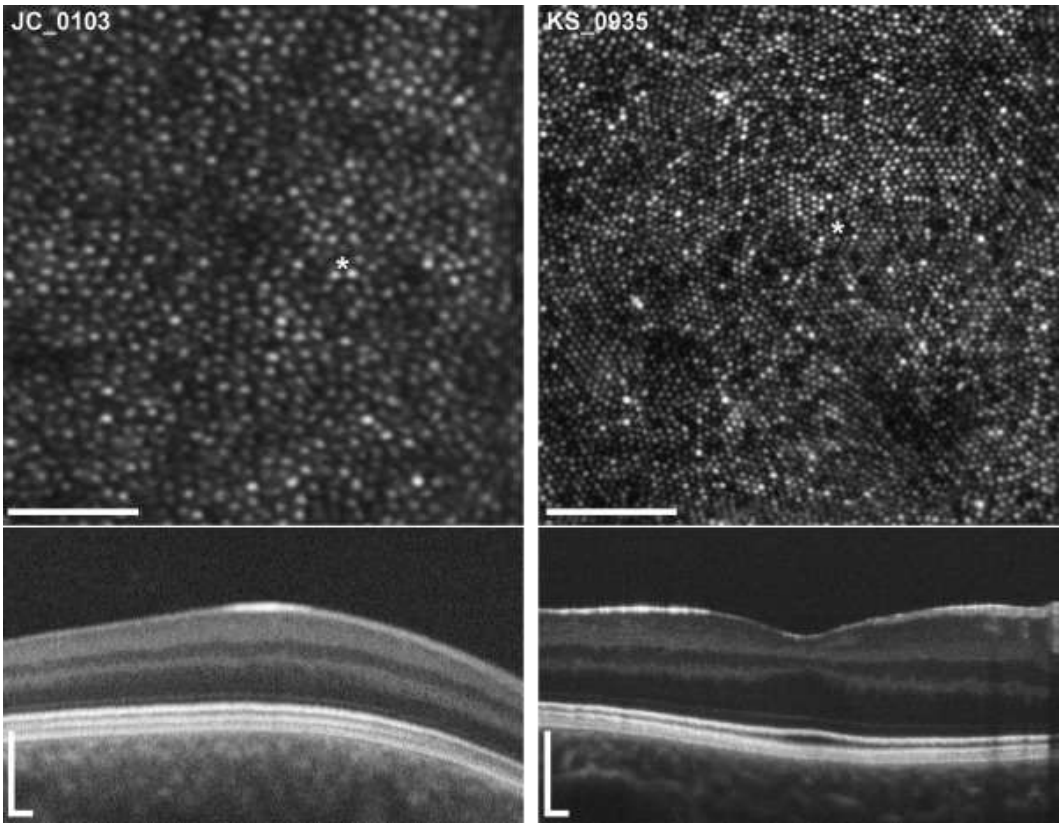

Fig. 3. Variability in foveal cone specialization in patients with albinism. Left panel shows the foveal cone mosaic and OCT from a patient with albinism who had the lowest peak cone density (JC_0103, peak density = 29,200 cones/mm^2). The images on the right are from the subject with albinism who had the highest peak cone density (KS_0935) of 126,400 cones/mm^2. OS lengths for these subjects are 26.3 and 39.4 μm, respectively. The asterisk (∗) in the top panel marks the location of peak cone density for each subject. AO image scale bars = 50 μm; OCT scale bars = 200 μm.

Vision Research, Vol 130 (January 2017): pg. 57-66. DOI.

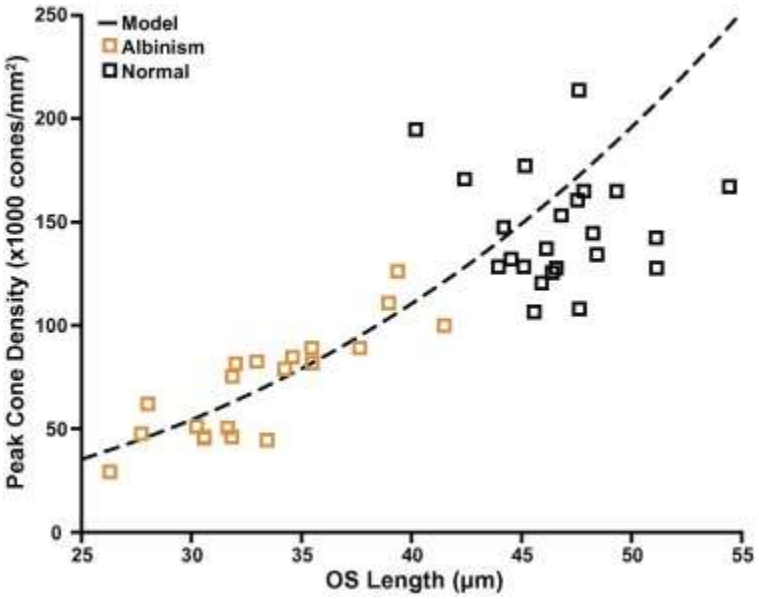

Fig. 4. Peak cone density and foveal OS length are correlated in albinism but not in normal retinas. Peak cone density is plotted against OS length. Orange squares represent subjects with albinism and open black squares are normal subjects. Peak cone density is significantly correlated with OS length in patients with albinism (Spearman r = 0.83; $p < 0.0001$) but not normal subjects (r = −0.002; p = 0.99). The model of the relationship between OS length and cone density in albinism is shown as the dashed black line, which fits the albinism data with an R^2 of 0.72. The OS lengths of normal subjects are generally greater than would be expected based on this model.

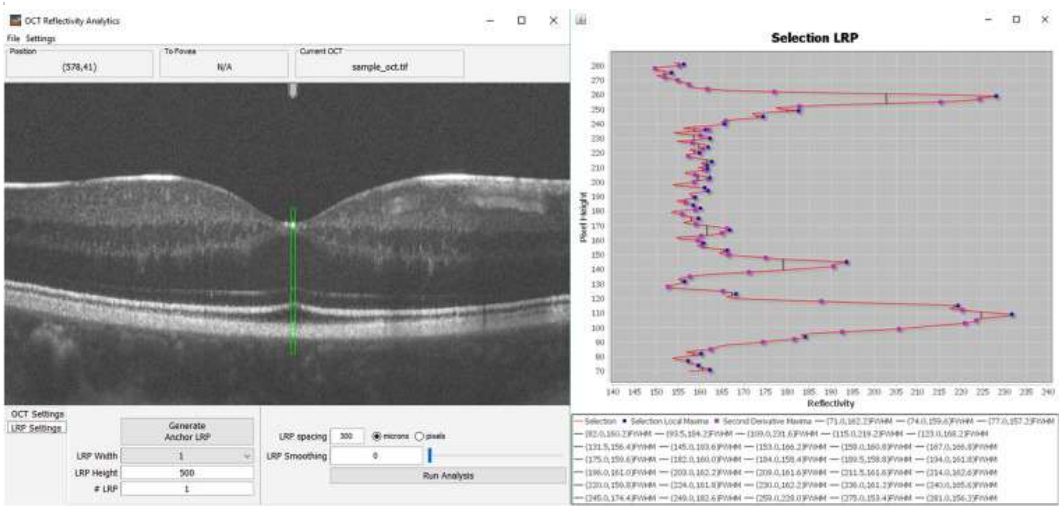

Fig. A.1. OCT Reflectivity Analytics (ORA) user interface. The main user interface is shown on the left with the corresponding, free-floating LRP graph on the right. The green box on the OCT image marks the region used for the LRP on the right. The second derivative peak detection algorithm detects local maxima as well as less apparent inflection points in the LRP that could be considered a peak (LRP – pink squares). The O(n) one dimensional peak detection algorithm detects elements where

the neighboring elements are less than the given element (LRP – blue dots). Black lines denote the full width at half maximum for the peaks marked with blue dots.

2.4. Modeling the relationship between cone density & OS length

To model the relationship between peak cone density and foveal OS length, the following assumptions were made: the OS is cylindrical and has a constant volume (V) of 141 μm^3 across subjects (Hoang et al., 2002, Yamada, 1969 and Yuodelis and Hendrickson, 1986); the ratio of OS width to inner segment (IS) width ($R_{OS/IS}$) varied linearly as a function of OS length (Eq. (1)), such that OS lengths (h_{OS}) of 25 μm had $R_{OS/IS}$ of 0.5 while OS length of 55 μm had $R_{OS/IS}$ of 0.75 (Hendrickson & Drucker, 1992); and the cone mosaic is arranged in a perfect crystalline lattice (Coletta & Williams, 1987).

equation(1)

$$R_{IS/OS} = \frac{25}{3} h_{OS} + \frac{7}{24}$$

For a range of OS lengths, the cone OS radius (r_{OS}) can be calculated as follows:

equation(2)

$$r_{OS} = \sqrt{\frac{V}{\pi h_{OS}}}$$

Cone OS radius (r_{OS}) was then converted to cone IS radius (r_{IS}) using an estimate of the OS/IS width ratio ($R_{OS/IS}$) from Hendrickson and Drucker (1992) as follows:

equation(3)

$$r_{IS} = \frac{r_{OS}}{R_{OS/IS}}$$

Cone IS radius can then be converted to cone [row] spacing (s_{row}), and subsequently density (D), as described by Coletta and Williams (1987):

equation(4)

$$s_{row} = r_{IS} \times \sqrt{3}$$

equation(5)

$$D = \frac{\sqrt{3}}{2 \times s_{row}^2}$$

A range of OS length measures that was comparable to the values measured in our subjects was used for the model (h_{OS} = 25–55 μm). A least squares approach was used to optimize the initial estimates of V and $R_{OS/IS}$ to fit the observed data.

3. Results

3.1. Variability in cone specialization

Cone density values for all 43 subjects are listed in Table 1. For normal subjects (n = 23), peak cone density ranged from 106,700 to 214,000 cones/mm^2 (average ± standard deviation = 147,000 ± 26,800 cones/mm^2; Fig. 2). These data are consistent with those from histology (Curcio et al., 1990) and previous in vivo imaging studies (Wilk et al., 2014b and Zhang et al., 2015). Consistent with previous reports (McAllister et al., 2010 and Wilk et al., 2014b), patients with albinism had much lower peak cone densities, ranging from 29,200 to 126,400 cones/mm^2 (71,100 ± 25,800 cones/mm^2; Fig. 3). OS length values in normal subjects averaged 46.8 ± 3.0 μm (40.2–54.5 μm), consistent with histology (Spaide and Curcio, 2011, Yamada, 1969 and Yuodelis and Hendrickson, 1986) and previous in vivo measurements (Srinivasan et al., 2008). On average, over the 500-μm region analyzed, the minimum OS length was 74% of the maximum OS length (range 63–81%). OS length at 2 mm from the maximum OS length was an average of 45% of the maximum (range 33–53%). Subjects with albinism had shorter foveal OS lengths, averaging 33.2 ± 4.0 μm (26.3–41.5 μm). Consistent with this, the average minimum OS length over the 500-μm region in these subjects was 88% of the maximum OS length (range 82–95%); for 2 mm eccentricity, the OS length was an average of 61% of the maximum OS length (range 34–83%).

Vision Research, Vol 130 (January 2017): pg. 57-66. DOI.

3.2. Relationship between cone density and OS length

We found that peak cone density was significantly correlated with OS lengths in patients with albinism ($p < 0.0001$; $r = 0.83$, Spearman rank correlation), but not in normal subjects ($p = 0.99$; $r = -0.002$). Given the lack of a relationship in normal subjects, and with our primary interest being in patients with albinism, our model was optimized for the albinism data alone (Fig. 4). Initial estimates of OS volume (V) of 141 μm^3 and $R_{OS/IS}$ of 0.5–0.75 for OS lengths of 25–55 μm provided a third-order polynomial model that fit the measured data with an R^2 of 0.69. Optimizing to fit our data, we found V to be 136.6 μm^3 and optimized $R_{OS/IS}$ ranged from 0.46 to 0.83 for OS lengths of 25–55 μm, still consistent with the literature. The optimized model provided an R^2 of 0.72 with the formula:

equation(6)

$$D = K(Ah_{OS}^3 + Bh_{OS}^2 + Ch_{OS})$$

with constants $A = 152.1111$, $B = 3.7419$ $C = 0.0230$, and $K = \frac{\sqrt{3}\times\pi}{6\times(136.6\times10^9)}$; and h_{OS} in mm. The majority of normal subjects fell to the right of the model, such that their densities were less than would be predicted from their OS length based on the albinism model.

4. Discussion

4.1. Implications

Patients with conditions such as albinism or aniridia present challenges for high-resolution imaging due to the presence of nystagmus. While our success rate for imaging foveal cones in subjects with nystagmus has been approximately 60% (Langlo et al., 2016), it leaves the other 40%, which may represent the more severe cases that could have unique foveal features, with no assessment of foveal cone density and structure. In patients like these, OCT becomes the only potential source of structural information about the photoreceptors. With the importance of the fovea for human vision, it is crucial that we are able to assess its specializations in any population. Therefore, the ability to estimate foveal cone density from

OS length in patients with albinism will allow for more in-depth analysis of albinism and its effects on foveal development.

Here we developed a model for estimating cone density from OS length in patients with albinism. While the model fits the albinism data quite well, a major consideration that is not accounted for in the model is the anatomical constraints on cone anatomy. While OS lengths shorter than what we report here have not been reported, few studies have thoroughly assessed the variability and range of cone anatomy of the adult human fovea (Hendrickson, 1992, Hendrickson and Drucker, 1992, Hendrickson et al., 2012, Hendrickson and Yuodelis, 1984 and Yuodelis and Hendrickson, 1986), and these assess only normal cone anatomy. It is reasonable to assume that, due to its basic stacked-disc structure, the OS cannot elongate indefinitely with increased packing (creating a ceiling effect for OS length). At this point, increases in cone packing would not be accompanied by further increases in OS length. Contrary to this reasoning, normal subjects showed no relationship between density and OS length, with the majority of subjects having cone density values less than would be expected based on their OS length (Fig. 4). The most likely reason for this is that some of the normal subjects' peak cone densities will be underestimated due to the inability to identify every cone in the mosaics of highest density. This is supported by the fact that in vivo AO-derived estimates of peak cone density, on average, fall below those reported from histology (Curcio et al., 1990, Gao and Hollyfield, 1992, Wilk et al., 2014b, Wilk et al., 2016 and Zhang et al., 2015). Despite the resolution of current AOSLO systems, tightly packed cones can cause interference of neighboring cones and therefore lower measured density values (Putnam, Hammer, Zhang, Merino, & Roorda, 2010). Improvements to cone identification could be made by averaging multiple images of the fovea from different time points to capture changes in cone reflectance, and/or by imaging with shorter wavelengths (Dubra et al., 2011). It would also be interesting to see if a strong relationship between density and OS length is seen in other populations with foveal hypoplasia, particularly in patients born prematurely who lack other pathology, which could clarify the disconnect observed here for normal subjects.

4.2. Limitations

While this work demonstrates the usefulness of OCT and OS length to estimate cone density, it is important to note that this technique requires that OCT images be acquired through the location of maximum OS length. The model also assumes that this location of maximum OS length corresponds to the location of peak cone density. Given the relatively low resolution of volumetric OCT compared to AOSLO, the inevitable error due to manual alignment of different imaging modalities, and that the highest cone density only occurs over an area as large as 0.032 deg^2 (Curcio et al., 1990), we were not able to confirm that the location of peak density was the same location as the maximum OS length. Given the strength of the relationship in albinism, as well as the general reduction in foveal cone density, it appears not to be an issue in this population. However, the lack of a clear relationship in normal subjects could be due to a misalignment of peak density and OS length. While the OCT device used here lacks the necessary lateral resolution, implementation of AO in OCT instruments could provide a solution to this problem. Not only does AO-OCT provide high axial resolution, its improved lateral resolution also enables the visualization of individual cone photoreceptors (Jonnal et al., 2012, Jonnal et al., 2010, Jonnal et al., 2014 and Zhang et al., 2006). En face images generated from AO-OCT have been shown to resolve individual cones as close to the fovea as 0.5 degrees (Kocaoglu et al., 2011), and Lee, Werner, and Zawadzki (2013) have provided evidence that such systems are capable of resolving rod photoreceptors with a theoretical lateral resolution under two microns. Furthermore, the combination of AO-OCT and SLO provides the ability to simultaneously obtain high-resolution cross-sectional and en face images (Zawadzki et al., 2011). This combination of cross-sectional and en face imaging, either through standalone AO-OCT or combination AO-OCT/SLO, could provide a mechanism with which to measure OS length and cone density at the same location in normal subjects. While the patients with albinism may not require AO-OCT to assess the relationship between cone density and OS length (as seen by the strong relationship here), application of AO-OCT to this population may also improve the accuracy of our measurements in this population. However, to our knowledge, AO-OCT has not been used to

Vision Research, Vol 130 (January 2017): pg. 57-66. DOI.

assess the foveal cones in normal individuals, nor has it been attempted in patients with albinism.

In addition, differences in segmentation methods could result in different measures of OS length (Stepien, Kay, & Carroll, 2014), highlighting the importance of standardized analyses for image segmentation when comparing data across different studies. While peak reflectance often corresponds to the center of a given band, this is not always the case. A blurring of IZ and RPE bands occurs at the fovea, which is more apparent in normal individuals compared to patients with albinism who have reduced melanin (Wilk et al., 2014b). These differences in reflectance may affect the relative location of peaks in these two populations and subsequently may alter the measures of OS length from LRPs. More work is needed to refine the methods for more accurate measurement of OS length in vivo.

4.3. Conclusions

Based on histological assessment of cone specialization, and optimized for the correlation observed here, we were able to develop a model for the relationship between foveal OS length and cone density in patients with albinism. While the model provides a good estimate of foveal cone density in this population, normal subjects showed no relationship between cone density and OS length. Refinement of methods and additional work in other patients with foveal hypoplasia (such as individuals born prematurely, who would lack other underlying pathology) may provide insight into the discrepancy between these two populations.

Disclosures

MA Wilk, None; BM Wilk, None; CS Langlo, None; RF Cooper, None; J Carroll, None

Acknowledgments

The authors thank Alfredo Dubra, Brian Higgins, Mara Goldberg, and Phyllis Summerfelt for their contributions to this work, as well as Gail Summers, Deborah Costakos, Thomas Connor, Kimberly Stepien, and William Wirostko for patient referrals. Research reported in this publication was supported by

the National Eye Institute and the National Institute of General Medical Sciences of the National Institutes of Health under award numbers T32EY014537, T32GM080202, P30EY001931, R01EY017607, and R01EY024969. This investigation was conducted in a facility constructed with support from Research Facilities Improvement Program, Grant Number C06RR016511, from the National Center for Research Resources, National Institutes of Health. The content is solely the responsibility of the authors and does not necessarily represent the official views of the National Institutes of Health. This work was also supported by Vision for Tomorrow; the Edward N. & Della L. Thome Memorial Foundation, Bank of America, N.A. Trustee; the Gene & Ruth Posner Foundation; and an unrestricted departmental grant from Research to Prevent Blindness, Inc., New York, NY to the Department of Ophthalmology at the Medical College of Wisconsin.

Appendix A. OCT Reflectivity Analytics (ORA)

ORA is a tool that allows users to manipulate OCT images, generate multiple LRPs, and analyze reflectance information with a similar approach as Hammer et al. (2008). It was developed in Java (Java v1.8, Oracle Corporation, Redwood Shores, CA) to improve its portability across platforms while maintaining ease of use. The user interface (Fig. A.1) was designed to interact with users and enhance their ability to analyze OCT images in a consistent and reproducible manner. The workflow described below requires an input image, setting of analysis parameters, interacting with LRPs, and exporting the results.

A.1. Input

Users select logarithmic B scan images, saved as '.TIFF' files. Horizontal and vertical scaling measurements (for converting between pixels and microns) should be known and can be entered under the "OCT Settings" tab prior to analyzing the image. ORA was initially developed to analyze Bioptigen OCT images. An important consideration for input images is that different OCT devices might modify image contrast differently (e.g., Spectralis [Heidelberg Engineering, Heidelberg, Germany] is much different than Bioptigen OCT). While assessing peak-to-peak distances is not affected by the differences in the images from different devices, use of reflectance values requires knowledge of the manufacturer's process for creating the OCT images in order to accurately convert to linear images (Sundaram et al., 2014). Further development of ORA will extend the

usability to other OCT devices, accounting for such differences (provided that manufacturers disclose the manipulation/processing applied to the raw images before making them available to the end-user). Following the successful loading of an OCT image into ORA, the application monitors the position of the mouse when over the OCT. It reports this information back to the user as a Cartesian coordinate, displayed above the image, allowing the user to correlate positions on the OCT with LRPs.

A.2. Analysis settings

A.2.1. OCT settings

Upon successful loading of an OCT image, the user has the ability to adjust various image settings under the "OCT Settings" tab. Two-dimensional smoothing, also known as blurring, can be performed on the OCT image. This blurring uses a Gaussian blur, which is the convolution of the reflectivity data with a Gaussian function. Specifically, ORA uses the Gaussian blur implemented by another Java based image manipulation software library, ImageJ (Schneider, Rasband, & Eliceiri, 2012). ORA provides an interactive slider that allows the user to change the radius of the decay function for the Gaussian distribution and interactively see how the smoothing changes the OCT and LRP(s).

In addition to smoothing, ORA also allows for OCT image sharpening. ORA's implementation is based on the ImageJ implementation of an unsharp mask, which subtracts a blurred copy of the image and contrast-adjusts to sharpen. The user is provided with an interactive set of sliders that allows them to change the radius of the decay function for the Gaussian distribution used by the blur operation and the weight of the sharpening (i.e., the weight of the subtraction of the blurred image from the original). Like the other image modifiers, the sharpener allows users to interactively refine their analyses and see how the sharpening changes the OCT and LRP(s).

Beyond smoothing and sharpening the image, ORA allows for transition between logarithmic and linear formats. The initial input to ORA is a logarithmic scaled OCT. ORA provides a radio button selector

that allows the user to switch between using the logarithmic and linear scaled versions of the OCT image. In addition to this logarithmic and linear adjustment, ORA also provides the ability to contrast adjust the reflectivity values in the OCT. This contrast adjustment is a normalization of the reflectivity values in the current OCT to a 0–255 scale. This tool allows the user to increase contrast when assessing an OCT. Similarly, ORA also provides a method by which noise in the reflectivity values can be reduced. Specifically this noise reduction technique aims to reduce the presence of salt and pepper noise in the image. This is accomplished by applying a median filter to the image. This filter replaces each pixel in the image with the median pixel value of itself and its nearest neighbors. With all adjustments, the LRPs are automatically updated. While these adjustments can be made, it should be noted that these are intended for viewing purposes only. All analysis should be completed on the unmodified image without any smoothing or sharpening.

A.2.2. LRP settings and fovea finding

The second tab option contains LRP settings. Here, the user selects the width, height, spacing, and number of LRPs to generate. Furthermore, ORA offers LRP smoothing through implementation of a low pass filter applied to the LRP signal. The user is provided an interactive slider that allows the user to change the cutoff frequency of the filter and see how this alters the LRP. The goal of the smoothing is to provide a one-dimensional method for smoothing the reflectivity information to aid in the interpretation of results. Unlike the OCT smoothing, this LRP smoothing does not affect the image. Again, it should be noted that all analysis should be completed on an un-smoothed LRP and the smoothing is simply to assist the user in identifying peaks and interpreting the LRP pre-analysis.

ORA requires a point of origin, or anchor point, upon which to generate LRPs. Using the "Generate Anchor LRP" button, the user has the option to either select the anchor point manually or use ORA's built-in assisted fovea finding tool and use the fovea as the anchor point. The aim of the assisted fovea finder is to aid the user in the identification of the center of the fovea. To accomplish this, ORA segments the OCT at the retinal pigment epithelium (RPE)-Bruch's membrane (BrM) band and the internal limiting membrane using a

previously described algorithm (Chiu et al., 2010) and takes the vertical difference at each pixel along the segments. It then calculates the first derivative of the difference using the Apache Commons Math package (https://commons.apache.org/proper/commons-math/) and locates the local maxima and minima of the first derivative. ORA finds all zero crossings between the maxima and minima in the first derivative of the difference and lets the user choose which one best represents the center of the fovea. If the identification algorithm fails to correctly characterize the center of the fovea, the user can also manually select the fovea.

A.3. LRP generation

One of the key features of ORA is its ability to generate LRPs dynamically. The location of the OCT from which reflectivity information is gathered is displayed as a rectangular selection overlying the OCT image (Fig. A.1, OCT – green box). The LRP plot (Fig. A.1, LRP – red contour) is then displayed as a free-floating interactive graph generated using the JFreeChart graphing library (http://www.jfree.org/index.html). The combination of these two elements enables a user to correlate features of the LRP with the OCT.

Once the anchor LRP selection is chosen, the corresponding LRP is generated. Modifications to the OCT and/or LRP settings are automatically reflected in the LRP. Users can also selectively zoom and review any portion of an active LRP during the analysis. At this point, the anchor LRP can be adjusted if necessary, and the OCT and LRP settings should be returned to the initial unmodified settings for analysis. A second button under the "LRP Settings" tab is the "Run Analysis" button. Once selected, the LRPs are generated one at a time, starting with the leftmost LRP, and all settings are locked in for the entire analysis.

A.4. Peak detection & interactive LRP analysis modes

Peak detection is done for each LRP and is completed using two different methods. The first method is a second derivative peak detection algorithm designed to look for local maxima as well as less apparent inflection points in the LRP that could be considered a peak

(Fig. A.1, LRP – pink squares). The second method is a O(n) one dimensional peak detection algorithm, which looks for elements where the neighboring elements are less than the given element, with an extra condition that treats flat peaks (i.e., multiple consecutive points that collectively form a peak) as a single peak, centered in the middle of the flat peak (Fig. A.1, LRP – blue dots). Post-peak identification, the full width at half maximum (FWHM) is also calculated for all peaks identified by the second peak detection algorithm (Fig. A.1, LRP – black lines).

When hovering over a peak, its corresponding location on the image will be marked. The user is able to select the peaks of interest and label (by right-clicking) each with preset tags (ILM, OPL, ELM, EZ, IZ, RPE, BrM) or with an "Other" option to allow insertion of a free-text tag. The user moves through each LRP until all have been labeled. ORA determines the FWHM for each labeled peak. In addition, it calculates the distance between each combination of peak pairs. The combination of calculations provides the thickness of all structures selected during analysis, which can then be exported as outlined below.

The user has the choice to display certain information prior to and during analysis. These display options are located under the menu bar "Settings" tab and include the OCT file name, scale bars, LRP selection overlay, LRP peaks, and FWHM.

A.5. Output

Following the completion of an analysis, ORA also provides the user with the ability to save their work and export all of the results for review in external applications. The first export format is an '.ora' file. The '.ora' file is a textual representation of all the analysis information (including the OCT itself) converted into JavaScript Object Notation (JSON, http://www.json.org/). In doing this, an analysis can be saved in its current state and opened at a later point with the exact same settings and information. However, saving information in this format is not helpful for downstream review or use of the information calculated by ORA. For this purpose, there is an export feature that will create the '.ora' file for the analysis but also produces comma separated values (CSV) files for each LRP, the list of peaks within each LRP, and

all relevant statistics and measurements from analysis (FWHM and peak-to-peak measurements). These export features allow a user to pause their analysis and resume later, review what was done to generate a given set of LRPs, and further analyze their data using other tools (e.g., MatLab or Excel) as desired.

Appendix B. Supplementary data

Supplemental Table 1: Albinism genetics

Vision Research, Vol 130 (January 2017): pg. 57-66. DOI.

Subject	Genetics
JC_0103	*GPR143* c.797T>C; p.L266P*
JC_0438	*SLC45A2* c.264delC (frameshift) *SLC45A2* c.1417G>A; p.G473S*
JC_0456	*OCA2* c.1327G>A; p.V443I *OCA2* c.1555delG (frameshift) *TYRP1* c.1103delA (frameshift)
JC_0492	*TYR* c.1147G>A; p.D383N *TYR* c.1217C>T; p.P406L
JC_0493	*TYR* c.1147G>A; p.D383N *TYR* c.1217C>T; p.P406L
JC_0829	*TYR* c.899A>C; p.N300T* *TYR* c.1217C>T; p.P406L *TYR* c.1467_1468insT (frameshift)
DC_0831	*TYR* c.1467_1468insT (frameshift) *TYR* c.1205G>A; p.R402Q *TYR* c.575C>A; p.S192Y
KS_0935	*TYR* c.1217C>T; p.P406L *TYR* c.961T>C; p.C321R*
JC_10042	*TYR* c.1147G>A; p.D383N *TYR* c. 1205G>A; p.R402Q
JC_10061	*OCA2* 2.7kb deletion (homozygous)
JC_10074	*OCA2* c.365C>T; p.T122I *OCA2* c.2207C>T; p.S736L
JC_10081	*OCA2* c.79G>A; p.G27R (homozygous)
JC_10092	*TYR* c.1118C>A; p.T373K *TYR* c. 1205G>A; p.R402Q *OCA2* c.1256G>A; R419Q
JC_10093	*GPR143* c.346T>G; p.C116G *TYR* c. 1205G>A; p.R402Q (homozygous)
TC_10110	*TYR* c.1205G>A; p.R402Q (homozygous) *OCA2* c.1256G>A; p.R419Q *OCA2* c.913C>T; p.R305W *HPS5* c.3293C>T; p.T1098I
JC_10192	*SLC38A8* c.794A>G; p.Y265C *TYR* c.1205G>A; p.R402Q
JC_10227	*OCA2* c.1327G>A; p.V443I
JC_10230	*TYR* c. 1265G>A; p.R422Q *TYR* c. 1205G>A; p.R402Q
JC_10278	*TYR* c.286_287insA (frameshift) *TYR* c. 1205G>A; p.R402Q

References

Braaf et al., 2013. B. Braaf, K.V. Vienola, C.K. Sheehy, Q. Yang, K.A. Vermeer, P. Tiruveedhula, ... J.F. de Boer. Real-time eye motion correction in phase-resolved OCT angiography with tracking SLO. *Biomedical Optics Express*, 4 (1) (2013), pp. 51–65

Chiu et al., 2010. S.J. Chiu, X.T. Li, P. Nicholas, C.A. Toth, J.A. Izatt, S. Farsiu. Automatic segmentation of seven retinal layers in SDOCT images congruent with expert manual segmentation. *Optics Express*, 18 (18) (2010), pp. 19413–19428

Chui et al., 2012. T.Y.P. Chui, Z. Zhong, H. Song, S.A. Burns. Foveal avascular zone and its relationship to foveal pit shape. *Optometry and Vision Science*, 89 (5) (2012), pp. 602–610

Coletta and Williams, 1987. N.J. Coletta, D.R. Williams. Psychophysical estimate of extrafoveal cone spacing. *Journal of the Optical Society of America. A, Optics and Image Science*, 4 (8) (1987), pp. 1503–1513

Cooper et al., 2011. R.F. Cooper, A.M. Dubis, A. Pavaskar, J. Rha, A. Dubra, J. Carroll. Spatial and temporal variation of rod photoreceptor reflectance in the human retina. *Biomedical Optics Express*, 2 (9) (2011), pp. 2577–2589

Cooper et al., 2016. R.F. Cooper, M.A. Wilk, S. Tarima, J. Carroll. Evaluating descriptive metrics of the human cone mosaic. *Investigative Ophthalmology & Visual Science*, 57 (7) (2016), pp. 2992–3001

Curcio et al., 1990. C.A. Curcio, K.R. Sloan, R.E. Kalina, A.E. Hendrickson. Human photoreceptor topography. *Journal of Comparative Neurology*, 292 (4) (1990), pp. 497–523

Diaz-Araya and Provis, 1992. C. Diaz-Araya, J.M. Provis. Evidence of photoreceptor migration during early foveal development: A quantitative analysis of human fetal retinae. *Visual Neuroscience*, 8 (6) (1992), pp. 505–514

Dubis et al., 2012. A.M. Dubis, B.R. Hansen, R.F. Cooper, J. Beringer, A. Dubra, J. Carroll. Relationship between the foveal avascular zone and foveal pit morphology. *Investigative Ophthalmology & Visual Science*, 53 (3) (2012), pp. 1628–1636

Dubis et al., 2009. A.M. Dubis, J.T. McAllister, J. Carroll. Reconstructing foveal pit morphology from optical coherence tomography imaging. *British Journal of Ophthalmology*, 93 (9) (2009), pp. 1223–1227

Dubra and Harvey, 2010. A. Dubra, Z. Harvey. Registration of 2D images from fast scanning ophthalmic instruments. B. Fischer, B. Dawant, C.

Lorenz (Eds.), *Biomedical image registration*, Springer-Verlag, Berlin (2010), pp. 60–71

Dubra et al., 2011. A. Dubra, Y. Sulai, J.L. Norris, R.F. Cooper, A.M. Dubis, D.R. Williams, *et al.* Noninvasive imaging of the human rod photoreceptor mosaic using a confocal adaptive optics scanning ophthalmoscope. *Biomedical Optics Express*, 2 (7) (2011), pp. 1864–1876

Gao and Hollyfield, 1992. H. Gao, J.G. Hollyfield. Aging of the human retina: Differential loss of neurons and retinal pigment epithelial cells. *Investigative Ophthalmology & Visual Science*, 33 (1) (1992), pp. 1–17

Garrioch et al., 2012. R. Garrioch, C. Langlo, A.M. Dubis, R.F. Cooper, A. Dubra, J. Carroll. Repeatability of in vivo parafoveal cone density and spacing measurements. *Optometry and Vision Science*, 89 (5) (2012), pp. 632–643

Hammer et al., 2008. D.X. Hammer, N.V. Iftimia, R.D. Ferguson, C.E. Bigelow, T.E. Ustun, A.M. Barnaby, A.B. Fulton. Foveal fine structure in retinopathy of prematurity: An adaptive optics Fourier domain optical coherence tomography study. *Investigative Ophthalmology & Visual Science*, 49 (5) (2008), pp. 2061–2070

Hendrickson, 2005. A. Hendrickson. Organization of the adult primate fovea. P.L. Penfold, J.M. Provis (Eds.), *Macular degeneration*, Springer-Verlag, Heidelberg (2005), pp. 1–20

Hendrickson and Drucker, 1992. A. Hendrickson, D. Drucker. The development of parafoveal and mid-peripheral human retina. *Behavioural Brain Research*, 49 (1) (1992), pp. 21–31

Hendrickson et al., 2012. A. Hendrickson, D. Possin, L. Vajzovic, C.A. Toth. Histologic development of the human fovea from midgestation to maturity. *American Journal of Ophthalmology*, 154 (5) (2012), pp. 767–778

Hendrickson, 1992. A.E. Hendrickson. A morphological comparison of foveal development in man and monkey. *Eye*, 6 (1992), pp. 136–144

Hendrickson and Yuodelis, 1984. A.E. Hendrickson, C. Yuodelis. The morphological development of the human fovea. *Ophthalmology*, 91 (6) (1984), pp. 603–612

Hoang et al., 2002. Q.V. Hoang, R.A. Linsenmeier, C.K. Chung, C.A. Curcio. Photoreceptor inner segments in monkey and human retina: Mitochondrial density, optics, and regional variation. *Visual Neuroscience*, 19 (2002), pp. 395–407

Jonnal et al., 2012. R. Jonnal, O.P. Kocaoglu, Q. Wang, S. Lee, D.T. Miller. Phase-sensitive imaging of the outer retina using optical coherence tomography and adaptive optics. *Biomedical Optics Express*, 3 (1) (2012), pp. 104–124

Jonnal et al., 2010. R.S. Jonnal, J.R. Besecker, J.C. Derby, O.P. Kocaoglu, B. Cense, W. Gao, ... D.T. Miller. Imaging outer segment renewal in living human cone photoreceptors. *Optics Express*, 18 (5) (2010), pp. 5257–5270

Jonnal et al., 2014. R.S. Jonnal, O.P. Kocaoglu, R.J. Zawadzki, S.H. Lee, J.S. Werner, D.T. Miller. The cellular origins of the outer retinal bands in optical coherence tomography images. *Investigative Ophthalmology & Visual Science*, 55 (12) (2014), pp. 7904–7918

Kocaoglu et al., 2011. O.P. Kocaoglu, S. Lee, R.S. Jonnal, Q. Wang, A.E. Herde, J.C. Derby, ... D.T. Miller. Imaging cone photoreceptors in three dimensions and in time using ultrahigh resolution optical coherence tomography with adaptive optics. *Biomedical Optics Express*, 2 (4) (2011), pp. 748–763

Langlo et al., 2016. C.S. Langlo, E.J. Patterson, B.P. Higgins, P. Summerfelt, M.M. Razeen, L.R. Erker, ... ACHM-001 Study Group. Residual foveal cone structure in *CNGB3*-associated achromatopsia. *Investigative Ophthalmology & Visual Science*, 57 (10) (2016), pp. 3984–3995

Lee et al., 2013. S.H. Lee, J.S. Werner, R.J. Zawadzki. Improved visualization of outer retinal morphology with aberration cancelling reflective optical design for adaptive optics – optical coherence tomography. *Biomedical Optics Express*, 4 (11) (2013), pp. 2508–2517

Li et al., 2010. K.Y. Li, P. Tiruveedhula, A. Roorda. Intersubject variability of foveal cone photoreceptor density in relation to eye length. *Investigative Ophthalmology & Visual Science*, 51 (12) (2010), pp. 6858–6867

Liu et al., 2015. Z. Liu, O.P. Kocaoglu, T.L. Turner, D.T. Miller. Modal content of living human cone photoreceptors. *Biomedical Optics Express*, 6 (9) (2015), pp. 3378–3404

McAllister et al., 2010. J.T. McAllister, A.M. Dubis, D.M. Tait, S. Ostler, J. Rha, K.E. Stepien, ... J. Carroll. Arrested development: High-resolution imaging of foveal morphology in albinism. *Vision Research*, 50 (8) (2010), pp. 810–817

Perez et al., 2014. Y. Perez, L. Gradstein, H. Flusser, B. Markus, I. Cohen, Y. Langer, ... O.S. Birk. Isolated foveal hypoplasia with secondary nystagmus and low vision is associated with a homozygous SLC38A8 mutation. *European Journal of Human Genetics*, 22 (5) (2014), pp. 703–706

Provis et al., 2013. J.M. Provis, A.M. Dubis, T. Maddess, J. Carroll. Adaptation of the central retina for high acuity vision: Cones, the fovea, and the avascular zone. *Progress in Retinal and Eye Research*, 35 (2013), pp. 63–81

Putnam et al., 2010. N.M. Putnam, D.X. Hammer, Y. Zhang, D. Merino, A. Roorda. Modeling the foveal cone mosaic imaged with adaptive optics

scanning laser ophthalmoscopy. *Optics Express*, 18 (24) (2010), pp. 24902–24916

Putnam et al., 2005. N.M. Putnam, H.J. Hofer, N. Doble, L. Chen, J. Carroll, D.R. Williams. The locus of fixation and the foveal cone mosaic. *Journal of Vision*, 5 (7) (2005), pp. 632–639

Rossi and Roorda, 2010. E.A. Rossi, A. Roorda. The relationship between visual resolution and cone spacing in the human fovea. *Nature Neuroscience*, 13 (2) (2010), pp. 156–157

Saffra et al., 2012. N. Saffra, S. Agarwal, J.P. Chiang, R. Masini, A. Bertolucci. Spectral-domain optical coherence tomographic characteristics of autosomal recessive isolated foveal hypoplasia. *Archives of Ophthalmology*, 130 (10) (2012), pp. 1324–1327

Samara et al., 2015. W.A. Samara, E.A. Say, C.T. Khoo, T.P. Higgins, G. Magrath, S. Ferenczy, C.L. Shields. Correlation of foveal avascular zone size with foveal morphology in normal eyes using optical coherence tomography angiography. *Retina*, 35 (11) (2015), pp. 2188–2195

Schneider et al., 2012. C.A. Schneider, W.S. Rasband, K.W. Eliceiri. NIH Image to ImageJ: 25 years of image analysis. *Nature Methods*, 9 (7) (2012), pp. 671–675

Spaide and Curcio, 2011. R.F. Spaide, C.A. Curcio. Anatomical correlates to the bands seen in the outer retina by optical coherence tomography: Literature review and model. *Retina*, 31 (8) (2011), pp. 1609–1619

Srinivasan et al., 2008. V.J. Srinivasan, B.K. Monson, M. Wojtkowski, R.A. Bilonick, I. Gorczynska, R. Chen, ... J.G. Fujimoto. Characterization of outer retinal morphology with high-speed, ultrahigh-resolution optical coherence tomography. *Investigative Ophthalmology & Visual Science*, 49 (4) (2008), pp. 1571–1579

Stepien et al., 2014. K.E. Stepien, D.B. Kay, J. Carroll. Outer segment length in different best disease genotypes–reply. *JAMA Ophthalmology*, 132 (9) (2014), p. 1153

Sundaram et al., 2014. V. Sundaram, C. Wilde, J. Aboshiha, J. Cowing, C. Han, C.S. Langlo, ... M. Michaelides. Retinal structure and function in achromatopsia: Implications for gene therapy. *Ophthalmology*, 121 (1) (2014), pp. 234–245

Tanna et al., 2010. H. Tanna, A.M. Dubis, N. Ayub, D.M. Tait, J. Rha, K.E. Stepien, J. Carroll. Retinal imaging using commercial broadband optical coherence tomography. *British Journal of Ophthalmology*, 94 (3) (2010), pp. 372–376

Wagner-Schuman et al., 2011. M. Wagner-Schuman, A.M. Dubis, R.N. Nordgren, Y. Lei, D. Odell, H. Chiao, ... J. Carroll. Race- and sex-related differences in retinal thickness and foveal pit morphology.

Investigative Ophthalmology & Visual Science, 52 (1) (2011), pp. 625–634

Wilk et al., 2016. M.A. Wilk, A.M. Dubis, R.F. Cooper, P. Summerfelt, A. Dubra, J. Carroll. Assessing the spatial relationships between fixation and foveal specializations. *Vision Research* (2016) http://dx.doi.org/10.1016/j.visres.2016.05.001 Epub ahead of print

Wilk et al., 2014a. M.A. Wilk, B. Higgins, R.F. Cooper, D.H. Scoles, K.E. Stepien, C.G. Summers, ... J. Carroll. Contrasting foveal specialization in disorders associated with foveal hypoplasia. *Investigative Ophthalmology & Visual Science*, 55 (13) (2014), p. 694

Wilk et al., 2014b. M.A. Wilk, J.T. McAllister, R.F. Cooper, A.M. Dubis, T.N. Patitucci, P. Summerfelt, ... J. Carroll. Relationship between foveal cone specialization and pit morphology in albinism. *Investigative Ophthalmology & Visual Science*, 55 (7) (2014), pp. 4186–4198

Williams and Coletta, 1987. D.R. Williams, N.J. Coletta. Cone spacing and the visual resolution limit. *Journal of the Optical Society of America. A, Optics and Image Science*, 4 (8) (1987), pp. 1514–1523

Yamada, 1969. E. Yamada. Some structural features of the fovea centralis in the human retina. *Archives of Ophthalmology*, 82 (2) (1969), pp. 151–159

Yanni et al., 2012. S.E. Yanni, J. Wang, M. Chan, J. Carroll, S. Farsiu, J.N. Leffler, ... E.E. Birch. Foveal avascular zone and foveal pit formation after preterm birth. *British Journal of Ophthalmology*, 96 (7) (2012), pp. 961–966

Yuodelis and Hendrickson, 1986. C. Yuodelis, A. Hendrickson. A qualitative and quantitative analysis of the human fovea during development. *Vision Research*, 26 (6) (1986), pp. 847–855

Zawadzki et al., 2011. R.J. Zawadzki, S.M. Jones, S. Pilli, S. Balderas-Mata, D.Y. Kim, S.S. Olivier, J.S. Werner. Integrated adaptive optics optical coherence tomography and adaptive optics scanning laser ophthalmoscope system for simultaneous cellular resolution in vivo retinal imaging. *Biomedical Optics Express*, 2 (6) (2011), pp. 1674–1686

Zhang et al., 2015. T. Zhang, P. Godara, E.R. Blancob, R.L. Griffin, X. Wang, C.A. Curcio, Y. Zhang. Variability in human cone topography assessed by adaptive optics scanning laser ophthalmoscopy. *American Journal of Ophthalmology*, 160 (2) (2015), pp. 290–300

Zhang et al., 2006. Y. Zhang, B. Cense, J. Rha, R.S. Jonnal, H. Gao, R.J. Zawadzki, ... D.T. Miller. High-speed volumetric imaging of cone photoreceptors with adaptive optics spectral-domain optical coherence tomography. *Optics Express*, 14 (10) (2006), pp. 4380–4394